

High magnetic field stability in a planar graphene-NbSe₂ SQUID

Ayelet Zalic^{1,2}, Takashi Taniguchi³, Kenji Watanabe⁴, Snir Gazit^{1,5}, and Hadar Steinberg^{1,2}

¹*The Racah Institute of Physics, The Hebrew University of Jerusalem, Jerusalem 91904, Israel*

²*The Center for Nanoscience and Nanotechnology, Hebrew University of Jerusalem, Jerusalem 91904, Israel*

³*International Center for Materials Nanoarchitectonics, National Institute for Materials Science, 1-1 Namiki, Tsukuba 305-0044, Japan*

⁴*Research Center for Functional Materials, National Institute for Materials Science, 1-1 Namiki, Tsukuba 305-0044, Japan*

⁵*The Fritz Haber Research Center for Molecular Dynamics, The Hebrew University of Jerusalem, Jerusalem 91904, Israel*

Abstract

Thin NbSe₂ retains superconductivity at high in-plane magnetic field up to 30 T. In this work we construct an atomically thin, all van der Waals SQUID, in which current flows between NbSe₂ contacts through two parallel graphene weak links. This fully planar device remains uniquely stable at high in-plane field. This enables tracing the evolution of the critical current interference patterns as a function of the field up to 4.5 T, allowing nm-scale sensitivity to deviation from a perfect atomic plane. We present numerical methods to retrieve asymmetric current distributions $J_0(\mathbf{x})$ from measured interference maps, and suggest a new application of the dual junction geometry to probe the current density in the absence of phase information. The interference maps exhibit a striking field-driven transition, indicating a redistribution of supercurrent to narrow channels. Our results suggest the existence of a preferred conductance channel with enhanced stability to in-plane magnetic field.

Transition metal dichalcogenide (TMD) superconductors such as NbSe₂ can be mechanically exfoliated to yield thin layers down to the monolayer limit [1, 2]. Thin NbSe₂ superconducting electrodes sustain very high in-plane magnetic fields (B_{\parallel}) beyond the Pauli limit, due to suppressed orbital depairing and Ising spin orbit coupling (ISOC) which locks spins in the out of plane orientation [1]. The superconducting gap persists nearly unchanged up to 10 T [3], and remains observable up to 25 T in tunneling measurements [4].

It is useful to incorporate thin TMD superconductors in devices which utilize their unique properties at high B_{\parallel} . NbSe₂ has been coupled laterally to graphene to realize NS junctions [5, 6]. Devices consisting of NbSe₂ flakes coupled on both sides of a narrow graphene channel (Fig. 1a) are well-behaved Josephson junctions (JJs) [7, 8]. Our two dimensional planar Josephson junctions (2DJJs), constructed

exclusively from van der Waals (vdW) materials by transferring a cracked NbSe₂ flake on top of a graphene flake, are unique in retaining a Josephson effect at high parallel magnetic fields.

The Josephson effect occurs when supercurrent flows between two superconducting electrodes (in this case NbSe₂) connected by a weak link (graphene). Upon application of a small (mT scale for our devices) magnetic field perpendicular to the junction (B_{\perp}), the superconducting order parameter $\Delta e^{i\varphi}$ acquires a position-dependent phase and undergoes interference. This leads to a Fourier relation between the critical current $I_C(B_{\perp})$ and the maximal local critical current density $J_0(x)$ [9]:

$$I_C(B_{\perp}) = \left| \int_{-\infty}^{\infty} J_0(x) e^{ikx} dx \right| \quad (1)$$

where $k \equiv \frac{2\pi(2\lambda+d)B_{\perp}}{\phi_0}$, such that a loop connecting any two points x_1, x_2 , and extending across the junction length d into the superconductors up to the London penetration depth λ , encloses a magnetic flux of $k(x_2 - x_1)/2\pi$ in units of ϕ_0 (see Fig. 1d). In our previous work, we studied a 2DJJ subject to parallel fields as high as 8.5 T [8]. Even at such high fields, the highest accessible to our magnet, the device exhibits interference patterns.

The $I_C(B_{\perp})$ interference pattern holds information about the current density distribution within the junction, according to Eq. 1. However, extracting this information is difficult, since interference patterns reflect a variety of physical effects and require appropriate assumptions and methods to reconstruct the lost phase. Using such reconstructions, several groups have shown that current in graphene based Josephson junctions flows through the bulk with enhanced current density along the edges, while at the Dirac point edge channels dominate junction transport [10, 11].

In this work we extend the all-vdW 2DJJ concept to a SQUID geometry, with current flowing between NbSe₂ contacts through parallel monolayer graphene (MLG) and few-layer graphene (FLG) weak links (see Fig. 1b). In this highly planar structure, the graphene flakes are supported by a flat, insulating hexagonal boron nitride (hBN) substrate and all interfaces are atomically clean (see Fig. 1c). The device is gate tunable via a SiO₂ back-gate with traceable $I_C(B_{\perp})$ interference patterns up to $B_{\parallel} = 4.5$ T. The stability of the device allows us to extract the spatially varying current density as a function of gate voltage V_G and B_{\parallel} , revealing signatures of device geometry including a nm-scale step height between the MLG and FLG planes (see Fig. 1e).

At high B_{\parallel} the Fraunhofer envelope due to the current distribution within the MLG disappears, indicating a narrowing of the current channel. In order to extract the current density distribution, we address the phase retrieval problem using both a minimal parameter analytical fit, and a constrained maximum entropy fitting procedure. Further, we develop a new method relying on the Wiener Khinchin theorem, where a narrow junction serves to map the current density of a wider junction. Using these methods, we observe a gate-dependent spatial variation of current density in the MLG weak link at low field; at high B_{\parallel} our analysis corroborates the observed disappearance of the Fraunhofer envelope, confirming that current in the MLG focuses into a single narrow channel.

For our SQUID we use a single cracked NbSe₂ flake, of approximately 13 nm thickness, as seen in the cross-section TEM measurement (see supplementary); the length of both junctions, imposed by the NbSe₂ crack, is $d = 140$ nm in the direction of the current flow (see Fig. 1d). We measure dimensions

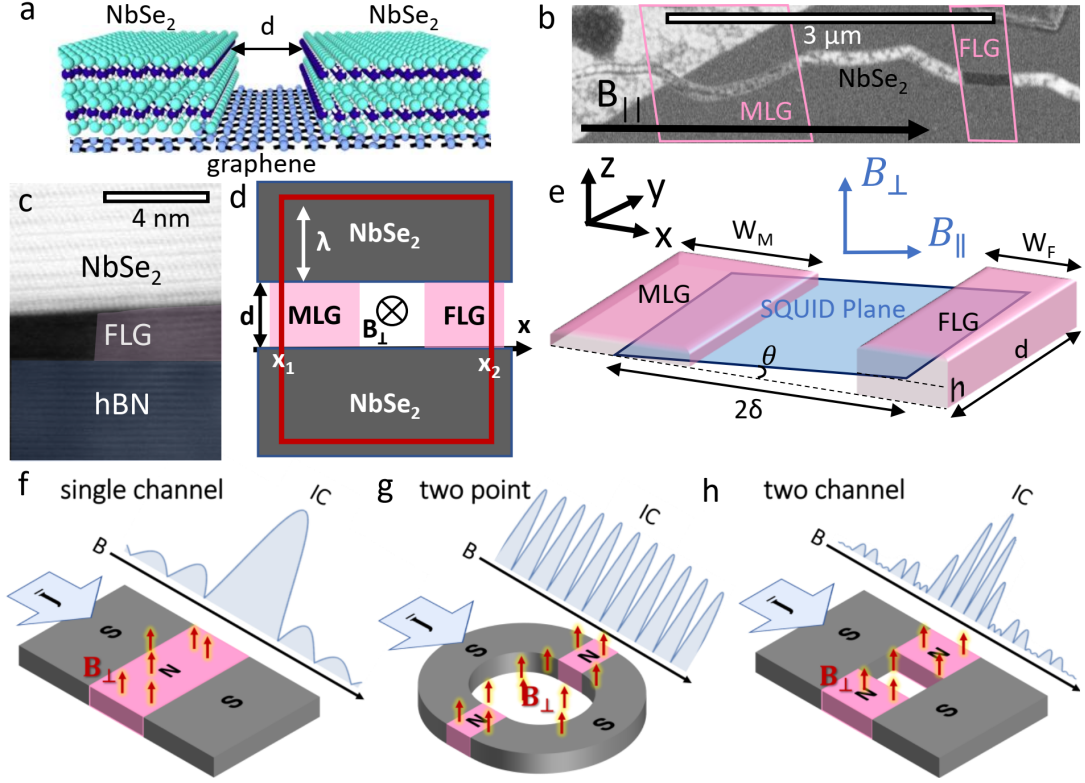


Figure 1: **a.** Planar NbSe₂-graphene-NbSe₂ JJ geometry **b.** SEM image of the device, flake outlines are a guide to the eye **c.** False-color cross-section TEM measurement of FLG region showing atomically clean interfaces between NbSe₂ and FLG, and between FLG and hBN **d.** Schematic showing B_{\perp} flux through one possible current circulation path, with an area $(2\lambda+d)|x_2 - x_1|$ **e.** Schematic illustration of FLG and MLG parallel weak links of different thicknesses. Directions \hat{x} and \hat{y} are in the plane of the flakes, \hat{z} is perpendicular. Mean SQUID plane is shown in blue, at an angle θ . B_{\parallel} is parallel to the SQUID plane and B_{\perp} is perpendicular to it. Crack length d is in the direction of current flow **f.-h.** Illustration of interference patterns for different junction geometries: **f.** single channel (Fraunhofer), **g.** two point (SQUID), and **h.** two channel (Fraunhofer envelope modulates SQUID oscillation).

using SEM, see Fig. 1b: the width of the MLG flake junction is $W_M \approx 1.45 \mu\text{m}$, while the width of the FLG junction is $W_F \approx 0.45 \mu\text{m}$. The distance between the centers of the two junctions is $2\delta \approx 2.7 \mu\text{m}$. For what follows, it is important to distinguish between different planes of reference in the sample. The magnetic field B_{\parallel} we refer to as “in-plane” is oriented parallel to the mean SQUID plane: the plane connecting the center of the MLG and FLG flakes (see Fig. 1e). This plane is at a small angle θ with respect to the plane of the MLG flake. Throughout the measurements reported here, B_{\parallel} is kept strictly aligned to the SQUID plane, for minimizing flux jumps. B_{\perp} is defined geometrically perpendicular to B_{\parallel} . Note that we control the field along the axes of the lab magnets, which are not exactly aligned with B_{\parallel} . We describe the compensation and alignment procedure in detail in the supplementary.

To gain initial insight into the expected $I_C(B_{\perp})$ in the SQUID, we make two simplifying assumptions: (i) the phase dynamics are local and (ii) the current-phase relation is sinusoidal. Both assumptions are typical for graphene-based JJs. However, ballistic graphene JJs may exhibit measurable skewness in

the current phase relation [12], while in ultrathin superconducting contacts, the Pearl length $\Lambda = 2\lambda_L^2/t$ replaces λ_L as the relevant field decay scale and the dynamics become potentially non-local [13]. We also approximate a spatially uniform current density in each channel. Applying Eq. 1 to this simplified model produces a two channel diffraction pattern [14] (see Fig. 1h), with the finite FLG/MLG widths (W_F, W_M) generating Fraunhofer-like envelopes (Fig. 1f) modulating the SQUID oscillations (Fig. 1g). The angle of the SQUID plane with respect to the MLG and FLG plane directly translates into a phase difference between the two channels. We describe the exact expression and the calculation leading to it in the supplementary material. Below, we refer to this as the ‘‘Analytical Model’’.

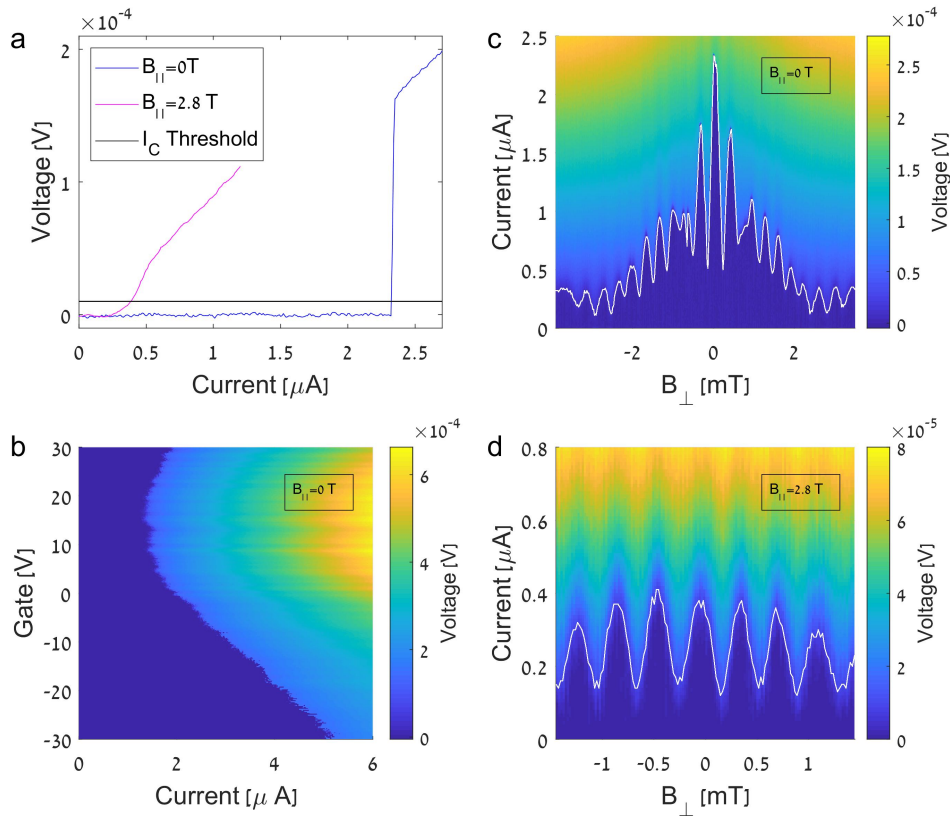


Figure 2: **a.** Current-voltage traces at $B_{\parallel} = 0$ T, $B_{\parallel} = 2.8$ T. Voltage threshold for determining critical current shown in black **b.** Current-voltage traces as a function of gate voltage at zero field. Gate modulates the critical current, with a minimum around 10 V (the MLG Dirac point) **c.** Interference pattern at $B_{\parallel} = 0$ T, with a $\Delta B \approx 380$ μ T oscillation corresponding to the SQUID area, and an envelope reflecting the area of the MLG and FLG junctions. A white line marks the threshold detection of I_C **d.** Interference pattern at $B_{\parallel} = 2.8$ T. The SQUID oscillation maintains similar periodicity to (a), but the envelope is no longer visible. Note measured B_{\perp} range at $B_{\parallel} = 2.8$ T is smaller than at 0 T to avoid entry of vortices

We begin by showcasing the basic properties of the 2D SQUID in Fig. 2. Current-voltage characteristics of the SQUID switch from zero to finite resistance at the critical current I_C , which we define according to a voltage threshold (see Fig. 2a). The transition from superconducting to normal conduc-

tance is sharpest at $B_{\parallel} = 0$ T. Panel (b) illustrates the modulation of critical current by varying charge carrier density. In our SQUID the common back-gate tunes both FLG and MLG densities simultaneously, therefore it is not possible to pinpoint the MLG Dirac point exactly (it is likely in the region of minimal I_C around 10 V).

The interference pattern of $I_C(B_{\perp})$ at zero gate voltage and $B_{\parallel} = 0$ T is shown in Fig. 2c. The rapid oscillations of I_C , with a magnetic field period $\Delta B = \phi_0 A_{SQ} \approx 380 \mu\text{T}$, reflect the area of the SQUID $A_{SQ} = 2\delta(2\lambda + d) = 5.4 \mu\text{m}^2$. This area implies an effective penetration length $\lambda = 930$ nm, longer than $\lambda_L \approx 200$ nm yet shorter than the Pearl length $\Lambda = 2\lambda_L^2/t \approx 6 \mu\text{m}$. The SQUID oscillations are modulated by an envelope which derives from the areas of the MLG and FLG channels, as illustrated by a schematic of two channel interference in Fig. 1h. Note that the measured $B_{\parallel} = 0$ T pattern is not perfectly symmetric with respect to B_{\perp} . This could be a signature of various symmetry breaking effects [15, 16], but is most likely due to vortices in the vicinity of the junction or a small trapped parallel flux.

The introduction of B_{\parallel} dramatically changes this pattern. At $B_{\parallel} = 2.8$ T (panel (d)), the SQUID oscillation persists and maintains its periodicity, whereas the envelope is no longer discernible. The data now resembles the two-point interference pattern in Fig. 1g. The contrast between zero and high field interference patterns is one of the main new results of our work. The transition to a two-point SQUID indicates a change in the supercurrent distribution, which becomes focused within a narrow channel at higher fields.

To investigate the supercurrent distribution systematically, we first turn to study how the $B_{\parallel} = 0$ T interference pattern evolves with respect to applied gate voltage, similarly to earlier works [10, 11]. We measure I_C as a function of B_{\perp} and V_G continuously, as shown in the color-plot in Fig. 3a. The data indicate that the overall SQUID periodicity remains fairly constant, whereas the critical current magnitude and the envelope change - indicating a variation in current distribution. Fig. 3d shows selected interference patterns from (a) at $V_G = -30$ V, 0 V, 30 V. We fit these curves using the analytical model described above, where the free parameters are the MLG and FLG widths W_M, W_F , the distance between their centers 2δ (see Fig. 1e), and the ratio between their critical current densities J_M/J_F (see supplementary for details).

Fig. 3e-g shows the current density profile for each V_G trace, extracted from the fit. For $2\lambda + d = 2 \mu\text{m}$, we find that fit parameters W_M, W_F, δ agree with the dimensions determined from SEM measurements shown in Fig. 1d (see comparison table in the supplementary). The model also indicates that the graphene channel exhibits a stronger response to the gate. The analytical curves fit the data reasonably well for the central lobes of the interference patterns - but the higher order lobes are far more pronounced in the data compared with the fit, hinting that the current density distribution has finer spatial detail beyond the two uniform conduction channels.

We thus turn to extract the current distribution in greater detail. Since the interference pattern reflects the absolute value of the Fourier transform of the current density, phase information is lost and it is impossible to directly apply an inverse Fourier transform. The oft-cited Dynes-Fulton approach to phase retrieval assumes a nearly symmetric current distribution, and so is not applicable in our case [17]. This approach is also not self-consistent, i.e. interference patterns generated from the extracted current

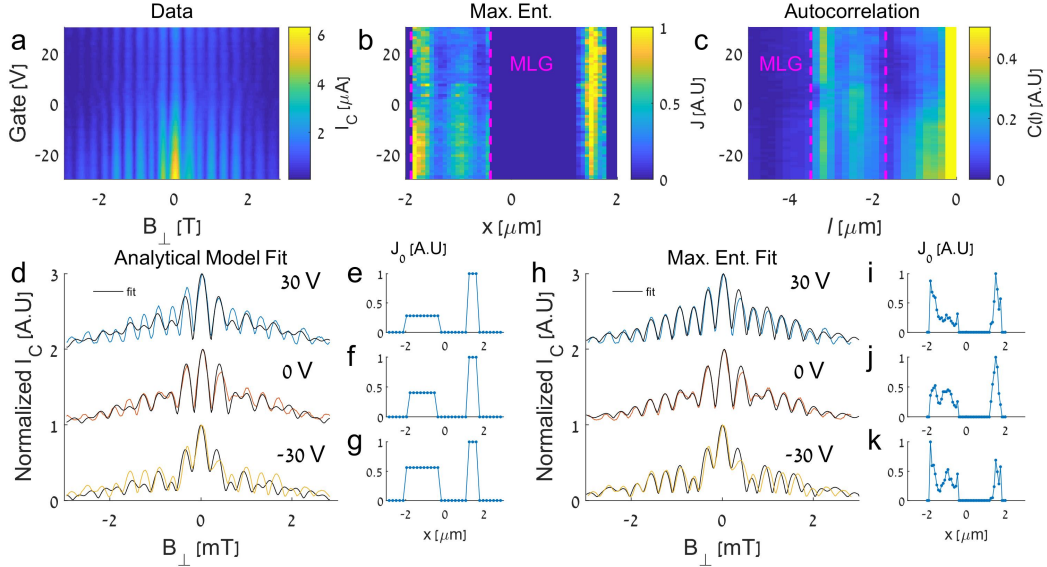


Figure 3: **a.** I_C (color scale) vs. B_{\perp} and gate voltage **b.** Normalized current density extracted from panel (a) using maximum entropy method **c.** Normalized autocorrelation function of the current density (color scale). Compare the side band to the MLG current density in panel (b) **d.** Interference patterns at gate voltages of -30, 0, 30 V with two channel analytical fit **e.-g.** Current density profiles corresponding to the analytical fits in panel (d) **h.** Interference patterns at gate voltages of -30, 0, 30 V with maximum entropy fit **i.-k.** Current density profiles corresponding to fits in panel (h)

distribution may not fit the original data [18].

An alternative method postulates a current density profile sampled at N discrete spatial points and subject to known physical constraints to calculate the critical current via a forward Fourier transform [18, 19]. The current density profile is then adjusted to obtain the best fit of the calculated interference pattern to the data. One work uses a constrained nonlinear optimization algorithm to minimize the least squares difference of the data and the fit [18]; another work adds a maximum entropy constraint in order to avoid spurious sharp changes in current density [19]. We use an approach inspired by the latter, which we term “the maximum entropy method” for future reference. See supplementary for the full details of our fitting algorithm, including our approach towards calibrating parameters and avoiding over-fitting (based on the L curve [20]).

Using the maximum entropy method, we extract the current density at $V_G = -30$ V, 0 V and 30 V, shown (normalized by the maximal J_0 for each gate) in Fig. 3i-k. To confirm self-consistency we apply Eq. 1 to reproduce the interference pattern corresponding to the extracted current density. We compare these to the measured patterns in Fig. 3h; the obtained fit is indeed far better than the analytical fit in Fig. 3d, especially in the higher order lobes. In panels i-k, the current within the MLG has two peaks; perhaps these are the edge channels observed in references [10, 11]. The color plot in Fig. 3b shows the full evolution of the extracted current density with gate voltage.

The maximum entropy fit is complex, with many algorithmic as well as physical parameters. This leads us to introduce a new method which uses the narrower FLG junction as a direct probe of the

current density in the wider MLG junction. This method leans on the Wiener Khinchin theorem, which states that the energy spectral density of a function and its autocorrelation $C(l)$ are Fourier transform pairs. In our case, $|I_C(B_\perp)|^2$ is the energy spectral density of $J_0(x)$, and thus:

$$F(|I_C(B_\perp)|^2) = C(l) = \int_{-\infty}^{\infty} J_0^*(x)J_0(x+l)dx \quad (2)$$

Consider a two channel device, where the current density in the one channel is narrow, approximated by the Dirac delta function, whereas the current in the other channel is widely distributed. The separation between the centers of the two channels is larger than their combined widths. The autocorrelation of the current density in this case contains a term equal to the current density in the wider channel (see calculation in the supplementary). In our case the FLG is only a few times narrower than the MLG, and carries a similar total current. In this instance, the autocorrelation convolves the FLG and MLG densities, resulting in a feature which qualitatively resembles the MLG current density “smeared” at the scale of the FLG width, and centered at $l = -2\delta$ equal to the distance between the centers of the two channels. Fig. 3c shows the autocorrelation ¹ as a function of gate; the resulting “side-band” centered at $l = -2.7 \mu\text{m}$ is qualitatively similar in its form to the extracted current density in Fig. 3b. We thus confirm that the autocorrelation method can be used to extract the current distribution, when one channel is narrow.

We now return to the field-driven transition shown in Fig. 2, using the methods discussed above to reconstruct the current distribution. Fig. 4 follows the same structure as Fig. 3. In panel (a) we plot $I_C(B_\perp, B_\parallel)$, tracing the evolution of the interference patterns as a function of parallel magnetic field at $V_G = 0 \text{ V}$. This interference plot is extremely stable, up to $B_\parallel = 4 \text{ T}$, barring minor flux jumps around $B_\parallel = 2.8 \text{ T}$, likely due to vortices entering the vicinity of the junction. There are two notable features seen in this data. First, the data exhibits a diagonal drift of the MLG envelope towards negative B_\perp . This is evident in a shift of maximal I_C , and of the first Fraunhofer nodes seen to intersect with the SQUID features. This shift is a direct result of device geometry: the step height h between MLG and FLG planes creates an angle θ between the SQUID plane and the MLG. With B_\parallel aligned to the SQUID plane, the flux through the MLG and FLG flakes receives a B_\parallel component, leading to the drift of the envelope (see full calculation in the supplementary). We note that the angle $\theta \approx 0.025^\circ$ extracted from the fit indicates a step height around 1 nm, while the TEM measured FLG thickness is 2.4 nm; this probably indicates a distribution of current throughout the FLG, with the mean SQUID plane determined by the center of the FLG flake. There could also be an additional step or curvature in the hBN outside the range of the TEM. The 2DJJ SQUID is thus an extremely sensitive tool for tracking deviations from atomic planar geometry.

Panel (b) shows current density extracted using the maximum entropy fit of an $I_C(B_\perp, B_\parallel)$ dataset.² The fit confirms that the current density in the MLG redirects into a narrow channel. The interference

¹The autocorrelation is smoothed as a result of zero-padding before calculating the discrete Fourier transform of $|I_C(B_\perp)|^2$.

²The data corresponding to the fit in Fig. 4 panel (b) is shown in supplementary Fig. S3; it is a different measurement containing a few more lobes in the interference pattern with respect to panel (a). This improves the spatial resolution of the extracted current density, but loses stability at lower B_\parallel .

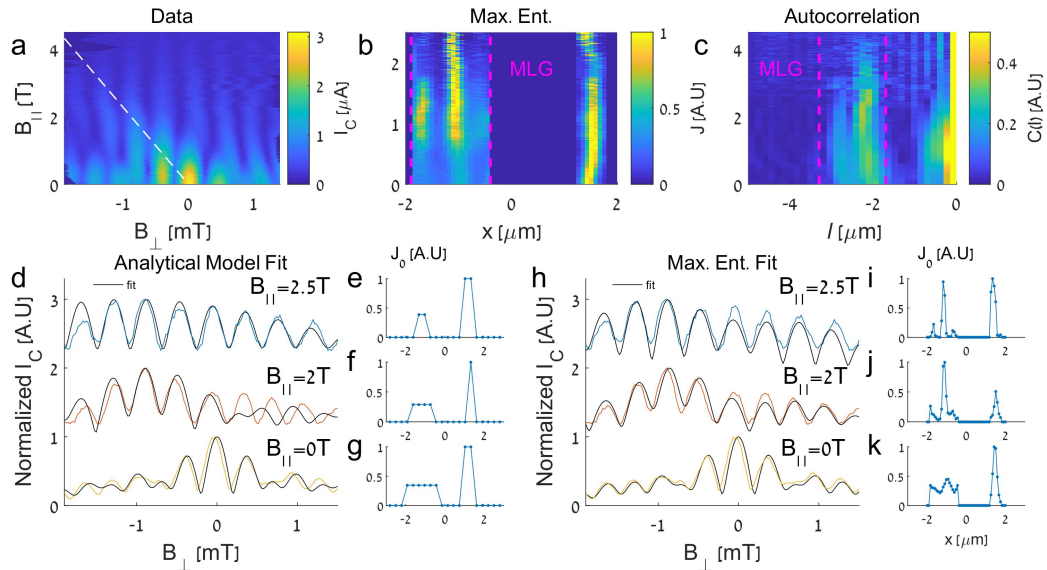


Figure 4: **a.** I_C (color scale) vs. B_{\perp} and B_{\parallel} . White dashed line marks the geometric angle $\theta \approx 0.025^\circ$ between the SQUID plane and the MLG **b.** Normalized current density extracted using the maximum entropy method **c.** Normalized autocorrelation function of the current density (color scale). Compare the side band to the MLG current density in panel (b) **d.** Interference patterns at B_{\parallel} 0 T, 2 T, 2.5 T with two channel analytical fit **e.-g.** Current density profiles corresponding to the analytical fits in panel (d) **h.** Interference patterns at B_{\parallel} 0 T, 2 T, 2.5 T with maximum entropy fit **i.-k.** Current density profiles corresponding to fits in panel (h).

patterns produced by the maximum entropy procedure fit most of the measured patterns closely, as shown for selected values of $B_{\parallel} = 0$ T, 2 T, 2.5 T in Fig. 4h. The extracted current densities at this succession of fields is depicted in Fig. 4i-k, illustrating the narrowing of the current carrying channel in the MLG as B_{\parallel} increases.³

This phenomenology is apparent also in our other methods of analysis. Panel (c) shows the autocorrelation of the current density. The side-band located around $l = 2.7 \mu\text{m}$ is qualitatively similar to the extracted MLG current density shown in Panel (b), and also exhibits a narrowing of the current channel in the MLG commencing at $B_{\parallel} = 2$ T. Panel (d) shows the best fit of our analytical model to interference patterns at $B_{\parallel} = 0$ T, 2 T, 2.5 T, while Fig. 4e-g show the current density profiles corresponding to the fit. Here too, the current density in the MLG grows narrower as B_{\parallel} increases. At low B_{\parallel} the analytical curve does not fit the data of the higher order lobes; but as B_{\parallel} increases the fit afforded by two uniform channels improves.

The transition towards narrow supercurrent channels has already been hinted at in our previous work - indeed, multiple diffusive MLG-NbSe₂ junctions also undergo a transition to SQUID-like interference patterns where all lobes are of similar height at high B_{\parallel} [8]. In that work however, the patterns were too disordered to fit to equation 1, and we could not rule out the role of ripples due to the SiO₂

³As the current channel grows narrow the pre-defined geometric constraint of the wide channel provides too much freedom, leading to reduction in the quality of the maximum entropy fit

substrate [8]. In the present work, the device is flat due to the use of an hBN substrate. In addition, the signal is sufficiently stable to allow quantitative fitting. All models, assuming an experimental geometry corroborated by SEM and TEM, yield a clear transition between a distributed current density in the MLG at low fields, to a narrow supercurrent channel at high B_{\parallel} .

We note that a similar effect of SQUID-like interference patterns at high B_{\parallel} , seen by Suominen et al., was attributed to suppression of supercurrent in the bulk of the JJ due to a magnetic dipole formed by tilted flux lines [21]. In our geometry however, SQUID-like interference indicates one channel in the MLG, not necessarily on the edge. Moreover, the model in [21] is relevant for magnetic fields oriented parallel to the current flow whereas our B_{\parallel} is perpendicular. The flux focusing effect is also weaker in thin NbSe₂ electrodes, where the tilt of the field lines is minimal due to a long London penetration length.

Thus in our devices, the origin of field-induced current re-distribution is an open question. The SQUID-like interference indicates the presence of a conductance channel with superior resilience to high B_{\parallel} . The suppression of a 2DJJ supercurrent vs. B_{\parallel} is determined by the interplay of the Thouless and Zeeman energy scales [22, 8]. The Thouless energy is a transport energy scale, determined by the inverse of the traversal time of the junction [23]. It supplants the superconducting gap as the determinant energy scale in a diffusive Josephson junction. Hence, the superior resilience of a single channel could be the consequence of a higher Thouless energy, if a particular channel allows faster traversal of the junction. This could be, for example, a guided edge mode, or a shorter channel in a non-uniform junction geometry. However, the presence of a similar effect in a number of devices suggests that it is not related to a particular geometry. Favored channels could also be the ones which experience minimal scattering in a disordered potential landscape. Alternatively, graphene could inherit Ising spin-orbit coupling by proximity to the NbSe₂ within the extended contact region between the two materials [24]. Such an interaction would enhance the stability of the carriers to in-plane field, and spatial variation of the induced coupling could lead to preferred channels. All in all, we find that the in-plane magnetic field appears to create narrow superconducting channels in graphene-NbSe₂ 2DJJs, an intriguing effect which has yet to be understood.

To conclude, the 2DJJ SQUID reported here is a novel experimental platform allowing us to measure interference patterns and extract current distributions at high B_{\parallel} , leading to interesting applications in sensing. It allows alignment of the parallel field to the SQUID plane at millidegree precision, and serves as an extremely sensitive probe for variation in the planarity of the current distribution in the weak links. Deviations from strict planar geometry may include substrate curvature and atomic height variation. Finally, we detect the presence of a supercurrent channel exceptionally stable to magnetic fields, raising important questions about the nature of the supercurrent in the graphene-NbSe₂ junction.

There is a recent surge of interest in planar JJs, realized in weak links with pronounced SO coupling. It is driven by the prospect of inducing $0-\pi$ transitions [25, 26], mapping spin textures using interference patterns [27, 28], and by predictions for topological effects tuned by parallel magnetic field [29, 30, 31, 32]. Looking to the future, it will be interesting to explore proximity effects in the 2DJJ and 2D SQUID. Within the extended contact region between the graphene and NbSe₂ leads (see Fig. 1a), graphene could

inherit Ising spin-orbit protection of the proximity superconducting gap [24, 33, 34]. Devices of this type would be useful in pinning down the role of the spin-orbit effect in the hybrid graphene-TMD structure.

1 Acknowledgements

The authors wish to thank Y. Anahory, M. Aprili, E. Grynszpan, N. Katz, A. Keselman, C. H. L. Quay and P. Ramachandran for insightful discussions. This work was funded by Israel Science Foundation Quantum Initiative grant 994/19, Israeli Science Foundation grant 861/19 and BSF grant 2016320. S.G. acknowledges support from the Israel Science Foundation, Grant No. 1686/18. A.Z. is grateful to the Azrieli Foundation for Azrieli Fellowships. K.W. and T.T. acknowledge support from JSPS KAKENHI (Grant Numbers 19H05790, 20H00354 and 21H05233).

2 Author contributions

A.Z fabricated the devices and performed the measurements, data analysis, analytical and numerical simulations. All authors contributed to the writing of the manuscript.

3 Competing financial interests

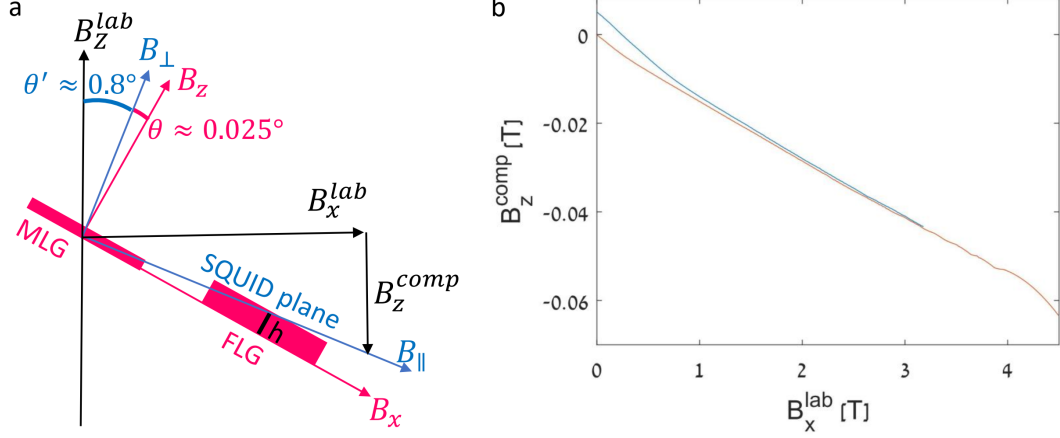
The authors declare no competing financial interests.

4 Methods

We exfoliate hBN on marked SiO₂ and locate substrate flakes of thickness around 20-40 nm. We exfoliate graphene to SiO₂ directly, and NbSe₂ first to PDMS and then stamp the PDMS on SiO₂ to transfer the flakes. This method supplies large, thin flakes of NbSe₂ which are not obtained by exfoliating directly from the blue tape to SiO₂. We use an optical microscope to search for two long, narrow graphene flakes which are within a few μm distance of each other for the channels of the SQUID, as well as NbSe₂ flakes which are a few layers thick and have an observable crack, less than 500 nm wide. We then employ a successive polycarbonate (PC) pickup technique [35] to pick up first the NbSe₂, then the graphene strips oriented perpendicular to the crack, and finally deposit the stack on the hBN substrate. We apply standard e-beam lithography and e-beam evaporation to create Ti/Au contacts to the NbSe₂, removing surface oxide using in-situ Argon ion milling prior to evaporation. Four-probe measurements were conducted in a BluFors dilution cryostat with a 3T/9T vector magnet and base temperature of 20 mK.

S1 Supplementary Section: Parallel field alignment procedure

Our SQUID is highly sensitive to perpendicular fields on the scale of tens of μT . This fact defines three relevant axes systems (see Fig. S1): the lab axis, along which we control B_z^{lab} and B_x^{lab} via our magnets;



Supplementary Figure S1: **a.** Three axes systems: in black, the “lab” axes along which magnetic field is controlled. In blue, the SQUID plane, oriented at $\theta' = 0.8^\circ$ with respect to the lab frame. In pink, the MLG plane, oriented at $\theta = 0.025^\circ$ with respect to the SQUID plane. Applying B_x^{lab} together with the compensation field B_z^{comp} creates B_{\parallel} in the SQUID plane **b.** B_z^{comp} as a function of B_x^{lab} for the data presented in Fig. S2c (blue) and main text Fig. 4 (orange)

the SQUID axis, with B_{\parallel} parallel to the SQUID plane and B_{\perp} perpendicular to it, and finally B_x, B_z which are parallel and perpendicular to the plane of the MLG, respectively. When applying magnetic field B_x^{lab} in the lab frame, stray perpendicular flux can penetrate the SQUID, either due to a small misalignment between the sample plane and the magnet axis, or from vortices or trapped magnetic flux in the leads, junction or the magnet itself. This leads to instability in the interference patterns, faster decay in the critical current with B_x^{lab} , and difficulty in interpretation of the results. We thus wish to apply high B_{\parallel} precisely along the SQUID plane, using the alignment procedure described below.

We calibrate $B = 0T$ in all directions and axes systems as zero applied field at cooldown. We then apply small B_z^{lab} and measure the interference pattern as a reference: at $B_x^{lab}=0T$, the interference pattern of the supercurrent has a clear maximum at $B_z^{lab}=0T$. Upon applying a small B_x^{lab} (say 10 mT) and subsequently measuring the interference pattern generated by B_z^{lab} , there will be a shift in the center of the pattern: since the center of the pattern is located at $B_{\perp} = 0T$, which no longer coincides with $B_z^{lab} = 0T$. To find the true state of zero flux through the SQUID, we assume a smooth evolution of the interference pattern with B_x^{lab} ; that is, small changes in B_x^{lab} will cause a minimal change/shift in the interference pattern of the junction. Based on this assumption, we find the shift in B_z^{lab} which maximizes the cross-correlation (implemented using Matlab xcorr function) between the measurement at $B_x^{lab} = 10mT$ and the reference at $B_x^{lab}=0T$. This shift is the compensation field B_z^{comp} , which we then take to be true $B_{\perp}=0T$. The pattern at 10 mT then serves as a reference for calculating the compensation field at 20 mT and so on. Fig.S1b shows the resulting compensation field as a function of B_x^{lab} for the measurements in Fig. S3c and Fig. 4 of the main text. The compensation algorithm along with the entire measurement is automated.

The angle $\theta' \approx 0.8^\circ$ between the z magnet axis and the normal to the SQUID plane is calculated from the ratio of the compensation field to B_x^{lab} . The angle between the MLG plane and the SQUID plane $\theta =$

0.025° is then inferred from a fit to the interference pattern as described in Supplementary Section 2. In the main text, as well as what follows in the supplementary, we approximate $B_{\parallel} = \sqrt{(B_z^{comp})^2 + (B_x^{lab})^2}$, and $B_{\perp} = B_z^{lab} - B_z^{comp}$. These approximations are accurate at least until second order in the small parameters $\theta, \theta', \frac{B_{\perp}}{B_{\parallel}}$.

The downside of this complicated alignment procedure is that it can also compensate for shifts in the interference pattern due to relevant physical causes, such as changes in the ground phase of the junction leading to a shift in the phase of the interference pattern (a 0- π transition for example). This information will not be apparent in a plot of I_C vs B_{\perp}, B_{\parallel} , such as the one presented in Fig. 4 of the main text. However the information is not lost, since we track the applied compensation field as a function of B_x^{lab} (see Fig. S1b). Note that there was trapped flux in the system in one of the measurements at $B_x^{lab} = 0T$, as evidenced by the finite compensation field. Note also that as B_x^{lab} approaches 4T, the compensation curve becomes non-linear; this is due to the automated cross-correlation algorithm gradually failing as the critical current descends below the minimal current detectable by the set voltage threshold.

S2 Supplementary Section: Analytical calculation of two channel interference pattern

The Josephson effect occurs when current flows between two superconducting electrodes (in this case NbSe₂) connected by a weak link. The proximity of the superconductors, under the correct conditions, allows a supercurrent to flow through the junction. Upon application of magnetic field perpendicular to the junction, the superconducting order parameter $\Delta e^{i\varphi}$ acquires a position-dependent phase and undergoes interference, resulting in a diffraction pattern of the critical current in magnetic field. The first Josephson relation relates the critical current density $J(x)$ to the phase difference between the order parameters of the two superconductors A and B, $\gamma(x) = \varphi_B(x) - \varphi_A(x)$:

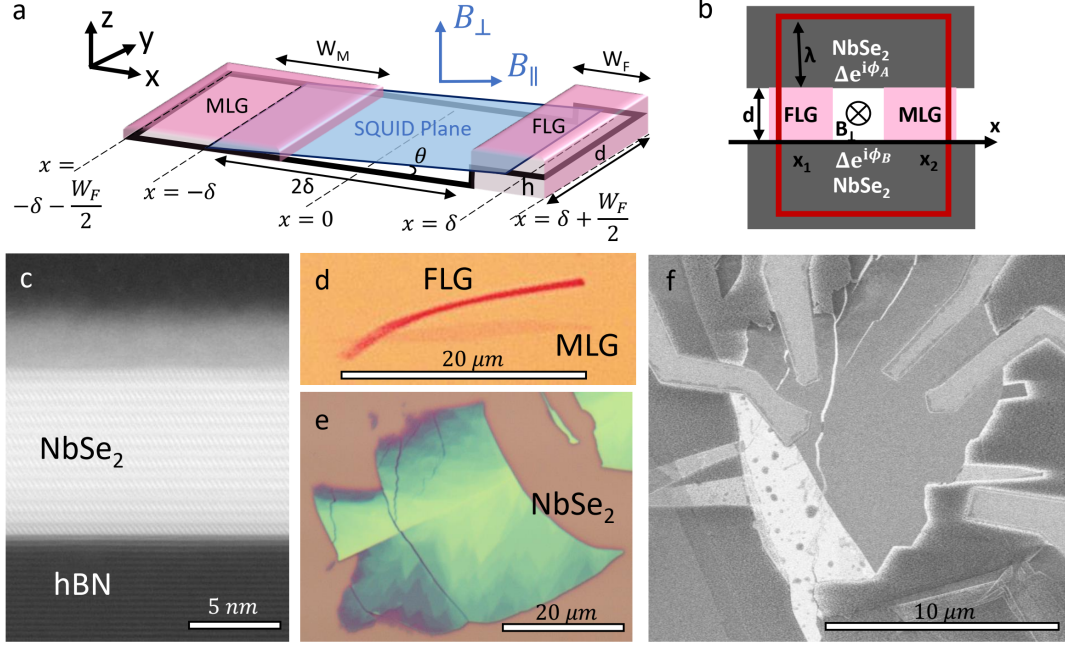
$$J(x) = J_0(x) \sin(\gamma(x)) \quad (\text{S1})$$

Here J_0 is the maximal possible critical current density at location x . The order parameter must retain a single-valued phase around any closed loop through which current may circulate, leading to the requirement:

$$\gamma(x_2) - \gamma(x_1) = \frac{2\pi\phi_A}{\phi_0} \quad (\text{S2})$$

Where ϕ_A is the magnetic flux through a loop connecting x_1, x_2 and extending across the junction length d into the superconductors up to the London penetration depth λ on either side (see Fig. S2b). For convenience we denote $L \equiv 2\lambda + d$.

Now we address our specific geometry. For this device we use NbSe₂ of thickness around 12-20 layers ($\approx 7-13$ nm). Fifteen layers are clearly seen in cross-section TEM measurement (Fig. S2c), below 3-5 nm of oxide; also from optical images, NbSe₂ thickness may vary slightly throughout the sample (Fig. S2e). The junction, of length $d=140$ nm in the direction of the current flow (y axis), has an MLG weak link



Supplementary Figure S2: **a.** Schematic illustration of FLG and MLG parallel weak links of different thicknesses and widths W_F, W_M respectively. Directions x and y are in the plane of the flakes, z is perpendicular. Mean SQUID plane is shown in blue, at an angle $\tan(\theta) = h/2\delta$. B_{\parallel} is parallel to the SQUID plane and B_{\perp} is perpendicular to it. **b.** Schematic showing B_{\perp} flux through one possible current circulation path, with an area $(2\lambda + d)|x_2 - x_1|$. Crack length d is in the direction of current flow. **c.** Cross-section TEM measurement of NbSe₂ on hBN. The top 4 nm of NbSe₂ are oxidized (amorphous, gray color), underneath are 15 visible layers **d.-e.** Enhanced contrast optical microscope images of graphene and NbSe₂ flakes, respectively, exfoliated on SiO₂ **f.** SEM image of the device.

of width $W_{MLG} \approx 1.45\mu\text{m}$ and an FLG weak link of width $W_{FLG} \approx 0.45\mu\text{m}$ and thickness $h=2.4$ nm (8 layers), their centers separated by a distance $2\delta \approx 2.7\mu\text{m}$. We define the x axis in the plane of the MLG/FLG flakes, perpendicular to current flow, and z perpendicular to the MLG/FLG plane. The magnetic field B_{\parallel} we refer to as “in-plane” is oriented parallel to the mean SQUID plane: the plane connecting the center of the MLG and FLG flakes. This plane is at a small angle $\tan(\theta) = \frac{h}{2\delta}$ with respect to the x axis. The field referred to as B_{\perp} is perpendicular to B_{\parallel} . This choice in alignment of B_{\parallel} maintains the peak of the central SQUID oscillation at $B_{\perp} = 0$ regardless of the applied B_{\parallel} (as described in Section S1). The applied field in x, z coordinates is as follows:

$$B_x = B_{\parallel} \cos(\theta) - B_{\perp} \sin(\theta) \approx B_{\parallel}, B_z = B_{\parallel} \sin(\theta) + B_{\perp} \cos(\theta) \approx B_{\parallel} \sin(\theta) + B_{\perp} \quad (\text{S3})$$

The approximations are to the first order in the small parameters θ and B_{\perp}/B_{\parallel} . The corresponding wave-numbers are:

$$k_1 = \frac{2\pi B_x (2\lambda + d)}{\phi_0}, k_2 = \frac{2\pi B_z (2\lambda + d)}{\phi_0} \quad (\text{S4})$$

We define a reference phase $\gamma_0 = \gamma(x = 0)$, with $x = 0$ at the center of the junction, such that the

centers of the MLG and FLG flake are both at the same distance δ from zero. Finally, the critical current is given by integrating over the current density $J_0(x)\sin(\gamma(x))$. We take care that the accumulated phase difference around a closed loop is always 0, accounting for the B_x flux exiting through loops with a vertical portion formed by the step h between the MLG and FLG:

$$I_C(B_\perp) = \max_{\gamma_0} \left(\int_{-\infty}^{\infty} J_M(x) \sin(\gamma_0 + k_2x) + J_F(x) \sin(\gamma_0 + k_2x - k_1h) dx \right) \quad (S5)$$

The integral can be written as the imaginary part of a complex exponential, and the whole expression becomes a Fourier transform:

$$I_C(B_\perp) = \max_{\gamma_0} \text{Im} \left(e^{i\gamma_0} \int_{-\infty}^{\infty} (J_M(x) + J_F(x)e^{-ik_1h}) e^{ik_2x} dx \right) = \left| \mathcal{F}(J_M(x) + J_F(x)e^{-ik_1h}) \right| \quad (S6)$$

To get a simple “zero-order” analytical expression for the critical current in our junction, we normalize the interference pattern by dividing by $I_C(B_\perp = 0)$, and assume a constant current density in each channel, with the ratio $\frac{J_F}{J_M} \equiv f$ an unknown parameter. Normalization of $I_C(B_\perp = 0)$ implies that $J_F W_F + J_M W_M = 1$, and leaves us with the following current densities expressed in terms of f, W_F, W_M :

$$J_F = 1/(W_F + 1/f * W_M); J_M = 1/f * J_F; \quad (S7)$$

Thus we obtain:

$$I_C(B_\perp) = \left| \mathcal{F} \left(J_M \text{rect} \left(\frac{x + \delta}{W_M} \right) + J_F \text{rect} \left(\frac{x - \delta}{W_F} \right) e^{-ik_1h} \right) \right| \quad (S8)$$

And the analytical expression for the interference pattern:

$$\begin{aligned} \frac{I_C(B_\perp)}{I_C(B_\perp = 0)} &= \sqrt{I_F^2 + I_M^2 + 2 * I_F * I_M * \cos(k_2 * 2\delta + k_1h)} \\ I_F &\equiv J_F W_F * \text{sinc}(k_2 W_F) \\ I_M &\equiv J_M W_M * \text{sinc}(k_2 W_M) \end{aligned} \quad (S9)$$

The angle of the SQUID plane with respect to the MLG and FLG plane translates into a phase difference between the two channels. Following is a tabulation of the fit parameters $W_M, W_F, 2\delta, \theta, h$ and their errors, extracted from a Matlab non-linear least squares fit of data shown in main text Figs. 3, 4 to the analytical model. The extracted dimensions may be compared to the measured dimensions given above. Note that there are different combinations of slightly different parameter values that can also yield a similar fit, therefore the true fit error is larger than the error bars given in the table.

V_g	B_\parallel	W_F	W_M	2δ	θ	h
0 V	0 T	330 ± 10 nm	1260 ± 25 nm	2720 ± 15 nm	X	X
-30 V	0 T	310 ± 20 nm	1590 ± 40 nm	2740 ± 20 nm	X	X
30 V	0 T	300 ± 15 nm	1600 ± 55 nm	2620 ± 30 nm	X	X
0 V	0 T	310 ± 50 nm	1500 ± 60 nm	2600 ± 35 nm	X	X
0 V	2.49 T	210 ± 20 nm	315 ± 40 nm	2500 ± 15 nm	$0.024 \pm 0.0003^\circ$	1.1 ± 0.01 nm

S3 Supplementary Section: Maximum entropy reconstruction of the current profile via Markov Chain Monte Carlo simulated annealing

In order to extract the current distribution in greater detail, we postulate an initial current density profile sampled at N discrete spatial points and subject to physical constraints, and calculate the corresponding interference pattern. We then adjust the density profile sequentially to obtain the best least-squares fit of the calculated interference pattern to the data, subject to a maximum entropy constraint. This is done via Markov chain Monte Carlo simulated annealing.

We begin by guessing a current density vector sampled at N points $\bar{J}_0 = [J_0(x_1), J_0(x_2) \dots J_0(x_N)]$ normalized such that $\sum_n J_x(x_n) = 1$. Valid guesses are constrained such that non-zero current density can exist only within the MLG and FLG channels, and current reversal (negative \bar{J}_0) is disallowed. We then calculate the corresponding interference pattern based on equation S9, with the perpendicular field sampled at M points $\bar{B}_\perp = [B_\perp^1, B_\perp^2 \dots B_\perp^M]$, B_\parallel set to some value, step height $h = 1$ nm and junction length $L = 2.2\mu\text{m}$ extracted from the analytical fit described in Section S2. Explicitly, we define the matrix element $A_n^m = \exp(i\frac{2\pi}{\phi_0}LB_z^m x_n)$ for $x_n < 0$, and $A_n^m = \exp(i\frac{2\pi}{\phi_0}L(B_z^m x_n - B_x^m h))$ for $x_n > 0$. We then compute:

$$I_C^{calc}(B_\perp^m) = \left| \sum_n A_n^m J_0(x_n) \right| \quad (\text{S10})$$

In order to quantify the fit of our guess \bar{J}_0 we calculate the least squares difference of $I_C^{calc}(B_\perp^m)$ with respect to the measured interference pattern $I_C^{meas}(B_\perp^m)$:

$$\chi^2(\bar{J}_0) = \sum_{m=1}^M (I_C^{calc}(B_\perp^m) - I_C^{meas}(B_\perp^m))^2 \quad (\text{S11})$$

We then sequentially adjust the fit by employing a Metropolis algorithm Markov chain Monte Carlo (MCMC) process which samples possible \bar{J}_0 configurations and assigns them a free energy reflecting a competition between the goodness of fit χ^2 and the entropy.

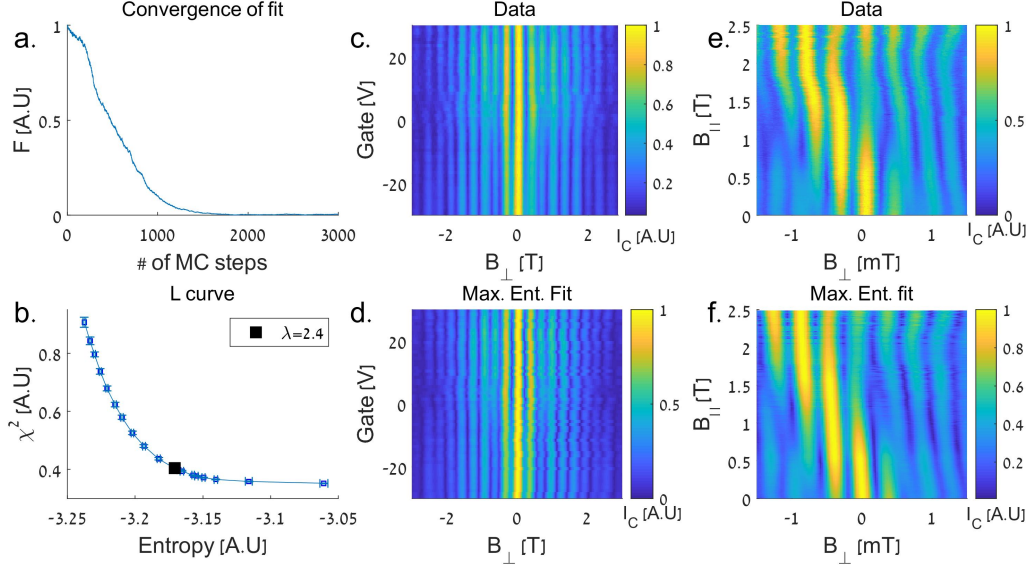
$$F(\bar{J}_0) = \chi^2(\bar{J}_0) + \lambda \sum_{n=1}^N J_0(x_n) \ln(J_0(x_n)) \quad (\text{S12})$$

Samples are correspondingly weighted with the standard Boltzmann weight $e^{-\beta F}$. The first term in the free energy penalizes a large deviation of the fit from the measurement, the second (entropy) term penalizes non-uniformity of the postulated current distribution, and the hyper-parameter λ tunes between them. A finite ‘‘temperature’’ $T = \beta^{-1} > 0$ introduces noise to the equilibrium current distribution but allows the algorithm to consider corrections to \bar{J}_0 which result in energy loss, and thus helps to avoid converging to local minima of χ^2 . In order to find the minimum of F , we employ simulated annealing, increasing the inverse temperature from 0 to β linearly with each Monte Carlo (MC) step. We ensure that \bar{J}_0 remains normalized by making changes in discrete units of size ΔJ ; a unit removed from site x_i must be added to some other site x_j . The steps of the algorithm are as follows:

1. Make an initial guess \bar{J}_0 obeying normalization and constraints.
2. Calculate $F(\bar{J}_0)$
3. Choose x_i, x_j at random from among the sites at which \bar{J}_0 is allowed to be non-zero. Propose $J'_0(x_i) = J_0(x_i) + \Delta J, J'_0(x_j) = J_0(x_j) - \Delta J$ so that the total current density is conserved.
4. If either $J'_0(x_i), J'_0(x_j)$ is negative, return to step 3. Otherwise, continue.
5. Calculate the new free energy $F_{new}(\bar{J}'_0)$
6. If $F_{new} < F$, accept new current density and return to step 3 updating $\bar{J}_0 \rightarrow \bar{J}'_0$. Otherwise, accept change $\bar{J}_0 \rightarrow \bar{J}'_0$ with probability $e^{-\beta_i(F_{new}-F)}$. The temperature at step i is given by $\beta_i = \beta/K * i$, where K is the total number of MC steps.
7. Return to step 3 and iterate K times.

We have freedom to change our initial guess \bar{J}_0 , and to tune the hyper-parameters $\lambda, \beta, N, \Delta J, K$. The x range of the simulation is defined between $\pm 2\mu m$, while the current in the MLG/FLG channels is bounded within the widths determined from the SEM measurement. Fourier uncertainty indicates that an interference pattern with N nodes yields a spatial resolution of $\frac{W}{N}$; that is, we can choose N evenly spaced discrete points to sample within the overall width W of the current carrying channels. However our fitting method is not an inverse Fourier transform; it introduces additional information through geometrical constraints as well as the maximum entropy constraint. Increasing the number of sampling points helps better fit the width and separation of the channels, while the maximum entropy constraint smooths any sharp spatial features. Thus, we choose $N = 50$, a few times larger than the bandwidth. We use a uniform initial distribution $\bar{J}_0 = \frac{1}{N^*}$, with N^* being the number of sample points allowed to carry current.

At zero magnetic field and maximal charge carrier density ($V_G = -1V$) we have measured a stable, nearly symmetric interference pattern with many lobes (see main text Fig. 3). We use this pattern to tune all of the hyper-parameters of the fitting algorithm. To tune the parameters $\beta, \Delta J$ we set $\lambda = 0$ and try several initial guesses for $\beta, \Delta J$ in powers of 10 before settling on $\beta = 10000, \Delta J = 0.001$ to obtain a convergence of F in a few thousand MC steps (see **S3a**). We note that any $10^3 < \beta$ and $\Delta J < 10^{-2}$ would work as well. We then choose $K = 5000$, several thousand MC steps after convergence. Finally, we tune λ by studying the L curve (see **S3b**), and choosing $\lambda = 2.4$ which provides a trade-off between decrease in goodness of fit and increase in entropy. Any λ in the vicinity (up to ≈ 6) gives a qualitatively similar current distribution, with smaller λ generating a noisier distribution and larger λ providing a poorer fit. As a sanity check, the spatial features of the current distribution generated by the fit do not have significant features on a length scale finer than that offered by the bandwidth of the original signal, as can be seen in Figs. 3, 4 of the main text. These parameters, chosen once based on the best data set, were then used to fit all of our measured data. See for example measured data of I_C vs. B_\perp and gate voltage (**S3c**) and I_C vs. B_\perp, B_\parallel (**S3e**), and compare to the fit in panels d,f. We note that there can in principle be multiple current distributions which give a comparable fit to the interference pattern,



Supplementary Figure S3: **a.** Convergence of the free energy as a function of MC steps **b.** The L curve, a parametric plot of χ^2 and entropy for different values of λ , with chosen $\lambda \approx 2.4$ marked **c.** Normalized I_C (color scale) vs. B_{\perp} and V_G **d.** Normalized I_C (color scale) vs. B_{\perp} and gate calculated using Eq. S6, with current density extracted from panel (a) by the Monte Carlo method **e.** Normalized I_C (color scale) vs. B_{\perp} and B_{\parallel} **f.** Normalized I_C (color scale) vs. B_{\perp} and B_{\parallel} from eq. S6, with current density extracted from panel (c) by the Monte Carlo method

due to the loss of phase information. However, fitting three different experimental repetitions of the B_{\parallel} measurement, changing the fitting hyper-parameters, changing initial conditions, etc. in the above described fitting procedure always results in similar current distributions if we use λ in the vicinity of the optimal λ determined by the L curve.

S4 Supplementary section: Current density extraction using the Wiener Khinchin theorem

The Wiener Khinchin theorem states that the energy spectral density of a function and its autocorrelation $C(l)$ are Fourier transform pairs. In our case, $|I_C(B_{\perp})|^2$ is the energy spectral density of $J_0(x)$, and thus:

$$F(|I_C(B_{\perp})|^2) = C(l) = \int_{-\infty}^{\infty} J_0^*(x)J_0(x+l)dx \quad (\text{S13})$$

Consider a two channel device, with the current density in the first channel very sharp and narrow, approximated by the Dirac delta function located at $x = a$, and the current density in the second channel given by some function F of finite width W centered at $x = -a$. The current density is thus: $J_0(x) = \delta(x - a) + F(x + a)$. The autocorrelation of the current density in this case is:

$$C(l) = \int_{-\infty}^{\infty} \delta(x-a)\delta(x-a+l) + F(x+a)F(x+a+l) + F(x+a)\delta(x-a+l) + F(x+a+l)\delta(x-a)dx \quad (\text{S14})$$

The first two terms give some function centered at $l = 0$. If we assume $W < a$, this function extends no further than $l = \pm W$. The second two terms give $F(2a \pm l)$: this is the current density of the second channel, centered at shifts equal to the distance between the two channels, $l = \pm 2a$ (and mirrored with respect to l around $l = 2a$). In our case the FLG is only a few times narrower than the MLG, and carries a similar current density. In this instance, the autocorrelation convolves the FLG and MLG densities, resulting in a feature which qualitatively resembles the MLG current density “smeared” at the scale of the FLG width, and centered at $l = -2\delta$ equal to the distance between the centers of the two channels.

References

- [1] Xiaoxiang Xi, Zefang Wang, Weiwei Zhao, Ju-Hyun Park, Kam Tuen Law, Helmuth Berger, László Forró, Jie Shan, and Kin Fai Mak. Ising pairing in superconducting NbSe₂ atomic layers. *Nature Physics*, 12(2):139–143, February 2016.
- [2] A. W. Tsen, B. Hunt, Y. D. Kim, Z. J. Yuan, S. Jia, R. J. Cava, J. Hone, P. Kim, C. R. Dean, and A. N. Pasupathy. Nature of the quantum metal in a two-dimensional crystalline superconductor. *Nature Physics*, 12(3):208–212, Mar 2016.
- [3] T Dvir, F Masee, L Attias, M Khodas, Marco Aprili, Charis H L Quay, and Hadar Steinberg. Spectroscopy of bulk and few-layer superconducting NbSe₂ with van der Waals tunnel junctions. *Nature Communications*, 9:598, 2018.
- [4] M. Kuzmanović, T. Dvir, D. LeBoeuf, S. Ilić, M. Haim, D. Möckli, S. Kraemer, M. Khodas, M. Houzet, J. S. Meyer, M. Aprili, H. Steinberg, and C. H. L. Quay. Tunneling spectroscopy of few-monolayer NbSe₂ in high magnetic field: Ising protection and triplet superconductivity. *arXiv*, arXiv:2104.00328, 2021.
- [5] D K Efetov, L Wang, C Handschin, K B Efetov, J Shuang, R Cava, T Taniguchi, K Watanabe, J Hone, C R Dean, and P Kim. Specular interband Andreev reflections at van der Waals interfaces between graphene and NbSe₂. *Nature Physics*, 12(4):328–332, April 2016.
- [6] Rai Moriya, Naoto Yabuki, and Tomoki Machida. Superconducting proximity effect in a NbSe₂/graphene van der Waals junction. *Phys. Rev. B*, 101:054503, Feb 2020.
- [7] Jongyun Lee, Minsoo Kim, Kenji Watanabe, Takashi Taniguchi, Gil Ho Lee, and Hu Jong Lee. Planar graphene Josephson coupling via van der Waals superconducting contacts. *Current Applied Physics*, 19(3):251–255, 2019.
- [8] Tom Dvir, Ayelet Zalic, Eirik Holm Fyhn, Morten Amundsen, Takashi Taniguchi, Kenji Watanabe, Jacob Linder, and Hadar Steinberg. Planar graphene-Nbse₂ Josephson junctions in a parallel magnetic field. *Phys. Rev. B*, 103:115401, Mar 2021.
- [9] M. Tinkham. *Introduction to Superconductivity*. International series in pure and applied physics. McGraw Hill, 1996.

- [10] M T Allen, O Shtanko, I C Fulga, A R Akhmerov, K Watanabe, T Taniguchi, P. Jarillo-Herrero, L S Levitov, and A Yacoby. Spatially resolved edge currents and guided-wave electronic states in graphene. *Nature Physics*, 12(2):128–133, feb 2016.
- [11] M. J. Zhu, A. V. Kretinin, M. D. Thompson, D. A. Bandurin, S. Hu, G. L. Yu, J. Birkbeck, A. Mishchenko, I. J. Vera-Marun, K. Watanabe, T. Taniguchi, M. Polini, J. R. Prance, K. S. Novoselov, A. K. Geim, and M. Ben Shalom. Edge currents shunt the insulating bulk in gapped graphene. *Nature Communications*, 8:6–11, 2017.
- [12] G. Nanda, J. L. Aguilera-Servin, P. Rakyta, A. Kormányos, R. Kleiner, D. Koelle, K. Watanabe, T. Taniguchi, L. M. K. Vandersypen, and S. Goswami. Current-phase relation of ballistic graphene Josephson junctions. *Nano Letters*, 17(6):3396–3401, Jun 2017.
- [13] Daniel Rodan-Legrain, Yuan Cao, Jeong Min Park, Sergio C. de la Barrera, Mallika T. Randeria, Kenji Watanabe, Takashi Taniguchi, and Pablo Jarillo-Herrero. Highly tunable junctions and non-local Josephson effect in magic-angle graphene tunnelling devices. *Nature Nanotechnology*, 16(7):769–775, Jul 2021.
- [14] R. C. Jaklevic, J. Lambe, J. E. Mercereau, and A. H. Silver. Macroscopic quantum interference in superconductors. *Phys. Rev.*, 140:A1628–A1637, Nov 1965.
- [15] Asbjørn Rasmussen, Jeroen Danon, Henri Suominen, Fabrizio Nichele, Morten Kjaergaard, and Karsten Flensberg. Effects of spin-orbit coupling and spatial symmetries on the Josephson current in SNS junctions. *Phys. Rev. B*, 93:155406, Apr 2016.
- [16] Alexandre Assouline, Cheryl Feuillet-Palma, Nicolas Bergeal, Tianzhen Zhang, Alireza Motaghizadeh, Alexandre Zimmers, Emmanuel Lhuillier, Mahmoud Eddrie, Paola Atkinson, Marco Aprili, and Hervé Aubin. Spin-Orbit induced phase-shift in Bi₂Se₃ Josephson junctions. *Nature Communications*, 10(1):126, January 2019.
- [17] R. C. Dynes and T. A. Fulton. Supercurrent Density Distribution in Josephson Junctions. *Phys. Rev. B*, 3:3015–3023, May 1971.
- [18] Hoi-Yin Hui, Alejandro M. Lobos, Jay D. Sau, and S. Das Sarma. Proximity-induced superconductivity and Josephson critical current in quantum spin Hall systems. *Phys. Rev. B*, 90:224517, Dec 2014.
- [19] Subhamoy Ghatak, Oliver Breunig, Fan Yang, Zhiwei Wang, Alexey A. Taskin, and Yoichi Ando. Anomalous Fraunhofer Patterns in Gated Josephson Junctions Based on the Bulk-Insulating Topological Insulator BiSbTeSe₂. *Nano Letters*, 18(8):5124–5131, Aug 2018.
- [20] Per Christian Hansen. Analysis of Discrete Ill-Posed Problems by Means of the L-Curve. *SIAM Review*, 34:561–80, Dec 1992.

- [21] H. J. Suominen, J. Danon, M. Kjaergaard, K. Flensberg, J. Shabani, C. J. Palmstrøm, F. Nichele, and C. M. Marcus. Anomalous Fraunhofer interference in epitaxial superconductor-semiconductor Josephson junctions. *Phys. Rev. B*, 95:035307, Jan 2017.
- [22] A. I. Buzdin. Proximity effects in superconductor-ferromagnet heterostructures. *Rev. Mod. Phys.*, 77:935–976, Sep 2005.
- [23] B. Pannetier and H. Courtois. Andreev reflection and proximity effect. *Journal of Low Temperature Physics*, 118(5):599–615, Mar 2000.
- [24] Martin Gmitra and Jaroslav Fabian. Graphene on transition-metal dichalcogenides: A platform for proximity spin-orbit physics and optospintronics. *Phys. Rev. B*, 92:155403, Oct 2015.
- [25] Chuan Li, Bob de Ronde, Jorrit de Boer, Joost Ridderbos, Floris Zwanenburg, Yingkai Huang, Alexander Golubov, and Alexander Brinkman. Zeeman-Effect-Induced $0-\pi$ Transitions in Ballistic Dirac Semimetal Josephson Junctions. *Physical Review Letters*, 123(2):026802, 2019.
- [26] Chung Ting Ke, Christian M Moehle, Folkert K Vries, Candice Thomas, Sara Metti, Charles R Guinn, Ray Kallaher, Mario Lodari, Giordano Scappucci, Tiantian Wang, Rosa E Diaz, Geoffrey C Gardner, Michael J Manfra, and Srijit Goswami. Ballistic Superconductivity and Tunable π Junctions in InSb Quantum Wells. *Nature Communications*, 10(1):3764, August 2019.
- [27] Sean Hart, Hechen Ren, Michael Kosowsky, Gilad Ben-Shach, Philipp Leubner, Christoph Brüne, Hartmut Buhmann, Laurens W Molenkamp, Bertrand I Halperin, and Amir Yacoby. Controlled finite momentum pairing and spatially varying order parameter in proximitized HgTe quantum wells. *Nature Physics*, 13(1):87–93, September 2016.
- [28] Angela Q Chen, Moon Jip Park, Stephen T Gill, Yiran Xiao, Dalmau Reig-i Plessis, Gregory J MacDougall, Matthew J Gilbert, and Nadya Mason. Finite momentum Cooper pairing in three-dimensional topological insulator Josephson junctions. *Nature Communications*, 9(1):3478, August 2018.
- [29] Falko Pientka, Anna Keselman, Erez Berg, Amir Yacoby, Ady Stern, and Bertrand I Halperin. Topological Superconductivity in a Planar Josephson Junction. *Physical Review X*, 7(2):021032, May 2017.
- [30] Hechen Ren, Falko Pientka, Sean Hart, Andrew T Pierce, Michael Kosowsky, Lukas Lunczer, Raimund Schlereth, Benedikt Scharf, Ewelina M Hankiewicz, Laurens W Molenkamp, Bertrand I Halperin, and Amir Yacoby. Topological superconductivity in a phase-controlled Josephson junction. *Nature*, 569(7754):93–98, April 2019.
- [31] Antonio Fornieri, Alexander M Whiticar, F Setiawan, Elías Portolés, Asbjørn C C Drachmann, Anna Keselman, Sergei Gronin, Candice Thomas, Tian Wang, Ray Kallaher, Geoffrey C Gardner, Erez Berg, Michael J Manfra, Ady Stern, Charles M Marcus, and Fabrizio Nichele. Evidence of topological superconductivity in planar Josephson junctions. *Nature*, 569(7754):89–92, May 2019.

- [32] William Mayer, Matthieu C. Dartiailh, Joseph Yuan, Kaushini S. Wickramasinghe, Enrico Rossi, and Javad Shabani. Gate controlled anomalous phase shift in Al/InAs Josephson junctions. *Nature Communications*, 11:212, January 2020.
- [33] J. O. Island, X. Cui, C. Lewandowski, J. Y. Khoo, E. M. Spanton, H. Zhou, D. Rhodes, J. C. Hone, T. Taniguchi, K. Watanabe, L. S. Levitov, M. P. Zaletel, and A. F. Young. Spin-orbit-driven band inversion in bilayer graphene by the van der Waals proximity effect. *Nature*, 571(7763):85–89, Jul 2019.
- [34] Yohanes S. Gani, Hadar Steinberg, and Enrico Rossi. Superconductivity in twisted graphene NbSe₂ heterostructures. *Phys. Rev. B*, 99:235404, Jun 2019.
- [35] P. J. Zomer, M. H. D. Guimarães, J. C. Brant, N. Tombros, and B. J. van Wees. Fast pick up technique for high quality heterostructures of bilayer graphene and hexagonal boron nitride. *Applied Physics Letters*, 105(1):013101, 2014.